Icarus 300 (2018) 115–128

Contents lists available at ScienceDirect

Icarus

journal homepage: www.elsevier.com/locate/icarus

Goldstone and Arecibo radar observations of (99942) Apophis in 2012–2013

Marina Brozović[a,*], Lance A.M. Benner[a], Joseph G. McMichael[a], Jon D. Giorgini[a], Petr Pravec[b], Petr Scheirich[b], Christopher Magri[c], Michael W. Busch[d], Joseph S. Jao[a], Clement G. Lee[a], Lawrence G. Snedeker[e], Marc A. Silva[e], Martin A. Slade[a], Boris Semenov[a], Michael C. Nolan[f], Patrick A. Taylor[g], Ellen S. Howell[f], Kenneth J. Lawrence[a]

[a] Jet Propulsion Laboratory, California Institute of Technology, 4800 Oak Grove Drive, Mail Stop 301-121, Pasadena, CA 91109-8099, USA
[b] Astronomical Institute, Academy of Sciences of the Czech Republic, Czech Republic
[c] University of Maine at Farmington, Preble Hall, Farmington, ME 04938, USA
[d] SETI Institute, Mountain View, CA 94043, USA
[e] SAITECH, Goldstone Deep Space Communication Complex, Fort Irwin, CA 92310-5097, USA
[f] University of Arizona, Tucson, AZ 85721, USA
[g] Arecibo Observatory, Universities Space Research Association, Arecibo, PR 00612, USA

ARTICLE INFO

Article history:
Received 12 April 2017
Revised 19 August 2017
Accepted 22 August 2017
Available online 30 August 2017

ABSTRACT

We report radar observations of Apophis obtained during the 2012−2013 apparition. We observed Apophis on fourteen days at Goldstone (8560 MHz, 3.5 cm) and on five days at Arecibo (2380 MHz, 12.3 cm) between 2012 December 21 to 2013 March 16. Closest approach occurred on January 9 at a distance of 0.097 au. We obtained relatively weak echo power spectra and delay-Doppler images. The highest range resolution was achieved at Goldstone, 0.125 μs or ∼20 m/px. The data suggest that Apophis is an elongated, asymmetric, and possibly bifurcated object. The images place a lower bound on the long axis of 450 m. We used the Pravec et al. (2014) lightcurve-derived shape and spin state model of Apophis to test for short axis mode (SAM) non-principal axis rotation (NPA) and to estimate the asteroid's dimensions. The radar data are consistent with the NPA spin state and they constrain the equivalent diameter to be $D = 0.34 \pm 0.04$ km (1σ bound). This is slightly smaller than the most recent IR observation estimates of $375^{(+14)}_{(-10)}$ m and 380–393 m, reported by Müller et al. (2014) and Licandro et al. (2016) respectively. We estimated a radar albedo of 0.25 ± 0.11 based on Goldstone data, and an optical albedo, p_V, of 0.35 ± 0.10. Licandro et al. (2016) reported p_V in the range of 0.24–0.33. The radar astrometry has been updated using a 3-D shape model. The Yarkovsky acceleration has not been detected in the current orbital fit, but if the position error during the 2021 encounter exceeds 8–12 km, this could signal a detection of the Yarkovsky effect.

1. Introduction

Near-Earth asteroid (NEA) (99942) Apophis (original designation 2004 MN4) was discovered on June 19, 2004 by R.A. Tucker, D.J. Tholen, and F. Bernardi at Kitt Peak in Arizona. Apophis was lost after two days and was rediscovered by the Siding Spring Survey in Australia in December of the same year. At the time of its recovery, the impact probability briefly reached 2.7% for the April 13, 2029 encounter with Earth, but it quickly diminished as the data arc increased. Detailed overviews of the events surrounding its discovery can be found in Giorgini et al. (2008) and Farnocchia et al. (2013).

Apophis will approach within five Earth radii of Earth's surface on April 13, 2029. This is the closest approach by an asteroid with an absolute magnitude of ∼19 or brighter known in advance. As a result of this passage, heliocentric semi-major axis will change from 0.92 au to 1.10 au, effectively reclassifying Apophis from the Aten to the Apollo family. Tidal interactions with Earth could change its spin state to a significant degree (Scheeres et al., 2005; Souchay et al., 2014) depending on the asteroid's spin axis orientation during the flyby. Major reshaping due to tides is unlikely (Scheeres et al., 2005; Yu et al., 2014) assuming that Apophis' bulk density is $> 1.5\,\mathrm{g\,cm^{-3}}$, a value comparable to those of other NEAs for which density estimates are available (Britt et al., 2002).

* Corresponding author.
E-mail address: Marina.Brozovic@jpl.nasa.gov (M. Brozović).

http://dx.doi.org/10.1016/j.icarus.2017.08.032
0019-1035/

Spectroscopy reported by Binzel et al. (2009) indicated that Apophis is an Sq-class object with a composition similar to the LL ordinary chondrites. Britt et al. (2002) list an average bulk density of 3.19 g cm^{-3} for LL ordinary chondrites. Yu et al. (2014) showed that only an encounter within two Earth radii is capable of triggering catastrophic avalanches of regolith and significant reshaping.

Apophis was detected with radar at Arecibo in 2005 and 2006 at distances of 0.192 au and 0.268 au from Earth (Giorgini et al., 2008). The signal-to-noise ratios (SNRs) were weak, only 4–7 standard deviations above the noise level. The opposite-circular (OC) radar cross-sections varied between 0.013 and 0.029 km^2 and hinted at an elongated shape. The circular polarization ratio was estimated to be 0.29 ± 0.15. Giorgini et al. (2008) reported that high precision radar astrometry consisting of five Doppler measurements and two round-trip-time measurements reduced the volume of the statistical uncertainty region for the 2029 encounter to 7.3% of the pre-radar solution. This estimate of the orbital uncertainties was assuming ballistic-only trajectory.

Lightcurves obtained by R. Behrend et al. in 2005 (https://obswww.unige.ch/~behrend/page_cou.html) provided the first evidence that Apophis has a slow, ~30.4 h rotation period. Behrend et al.'s lightcurve amplitude of 0.95 mag suggested that the asteroid is highly elongated. The most comprehensive study of Apophis' shape and spin state has been published by Pravec et al. (2014) based on an extensive set of lightcurves obtained between December 2012 and April 2013. Pravec et al. inverted lightcurves to obtain a convex shape model, but an absolute size of the model can only be estimated from the thermal or radar data. The Pravec et al. shape model is an elongated ovoid with wide and tapered ends. The ratio of the long to intermediate axes, a/b, is 1.44. The shape model derived from the lightcurves does not account for possible concavities. Pravec et al. also reported that Apophis is a non-principal axis (NPA) rotator in a short-axis mode (SAM) spin state with the precession and rotation periods $P_\phi = 27.38 \pm 0.07$ h and $P_\psi = 263 \pm 6$ h. From here, the main lightcurve frequency, ${P_1}^{-1} = {P_\phi}^{-1} - {P_\psi}^{-1}$, is 30.56 h.

Delbo et al. (2007) used polarimetry to estimate an absolute magnitude of $H_V = 19.7 \pm 0.4$, optical albedo of $p_V = 0.33 \pm 0.08$, and a diameter of $D = 0.27 \pm 0.06$ km. Pravec at al. (2014) reported an absolute magnitude of $H_V = 19.09 \pm 0.19$ mag which was used in recent thermal infrared studies by Müller et al. (2014) and Licandro et al. (2016) to obtain $p_V = 0.30^{+0.05}_{-0.06}$ and $p_V = 0.24$–0.33 respectively.

Studies by Müller et al. (2014) and Licandro et al. (2016) obtained effective diameters of 375^{+14}_{-10} m and 380–393 m, which was substantially larger than the initial Delbo et al. (2007) estimate. Both studies adopted the Pravec et al. shape and spin. Müller et al. (2014) reported a thermal inertia of $\Gamma = 600^{+200}_{-350}$ J m^{-2} $s^{-0.5}$ K^{-1} based on far-infrared observations by the Herschel Space Observatory. The thermal inertia was interpreted as evidence for a "mixture of low-conductivity fine regolith with larger rocks and boulders of high thermal inertia on the surface", similar to (25143) Itokawa. Licandro et al. (2016) extended the Müller et al. (2014) data set with mid-infrared observations from the Gran Telescopio CANARIAS in Spain and constrained the thermal inertia value to $\Gamma = 50$–500 J m^{-2} $s^{-0.5}$ K^{-1}.

The Yarkovsky effect is currently the dominant source of orbital uncertainty for Apophis (Giorgini et al., 2008; Farnocchia et al., 2013; Vokrouhlický et al., 2015). Modeling of the Yarkovsky acceleration involves a number of parameters such as the asteroid's spin state, size, surface density, and thermal conductivity. Vokrouhlický et al. (2015) showed that the orbital uncertainties for the 2029 encounter grow by an order of magnitude, from 6 km to 90 km, between gravity-only and gravity-and-Yarkovsky orbital fits. Furthermore, Vokrouhlický et al. (2015) noted that the inclusion of the Yarkovsky effect shifted the nominal orbital prediction by ~300 km in 2029. Vokrouhlický et al. (2015) found that the NPA rotation of Apophis does not significantly weaken the estimated Yarkovsky acceleration, which should lead to a secular change in the semimajor axis of $(-12.8 \pm 13) \times 10^{-4}$ au/Myr. This orbital change is not detectable at a significant level with current astrometry. A detection of the Yarkovsky acceleration would allow an estimation of the mass, and with a given diameter estimate from the thermal or radar observations would yield the bulk density. Constraints on the density would give some indication about the asteroid's internal structure, porosity, and possibly have implications for its collisional history.

2. Radar observations

Apophis approached Earth within 0.097 au on January 9, 2013, its closest encounter since 2004 and prior to 2029. The 2013 approach was at ~1/2 the distance relative to the radar observations in 2005 and ~1/3 relative to the distance in 2006. Thus, the SNRs in 2013 were significantly stronger. Using published results for the diameter, rotation period, and radar cross-section, we estimated daily SNRs of ~30 at Goldstone and ~50 at Arecibo for the 2012–2013 apparition, so we expected to obtain echo power spectra and coarse-resolution ranging measurements at Goldstone and echo power spectra and coarse resolution imaging at Arecibo.

We observed Apophis at Goldstone on 13 days between December 21, 2012 and January 17, 2013 and at Arecibo on 5 days between February 18 and March 16, 2013 (Table 1). Apophis approached from the south and the minimum distance occurred when the asteroid was too far south for Arecibo to track. The first radar detection during this encounter occurred during time originally scheduled to observe (4179) Toutatis when Apophis was at a declination of −27° and at distance of 0.103 au.

We used two observing setups: an unmodulated, Doppler-only, continuous waveform (CW) and a binary phase-coded (BPC) continuous waveform. We transmitted a circularly polarized electromagnetic wave that reflects off the target in the same sense of circular polarization (SC) as the outgoing beam and in the opposite sense (OC). Echoes from a surface that is smooth at decimeter scales will return almost entirely in the OC polarization. SC echoes can result from multiple scattering from rough surfaces, single scattering from surfaces with radii of curvature comparable to the radar wavelength, and from coherent backscattering. The ratio of the echo power strengths in SC and OC is a proxy for the target's near-surface complexity or roughness (Ostro et al., 2002).

The target's rotation spreads the signal in Doppler frequency. The Doppler broadening of the echo is defined as:

$$B = \frac{4\pi D}{\lambda P}\cos(\delta) \quad (1)$$

where B is the bandwidth, P is the rotation period, D is the diameter, λ is the radar wavelength, and δ is the subradar latitude.

The echo power spectra were processed with discrete Fourier transforms (DFT) and Welch's method (Welch, 1967). This approach estimates echo power spectra by dividing the time signals into 50% overlapping, windowed segments which ensures that no signal is lost. We used a Hamming window, which has a main lobe 1.47 times wider at 3 dB than the DFT resolution itself and results in a slight frequency smoothing. We tested this method against our standard non-overlapping processing (Magri et al., 2007) and found that the new method preserves the bandwidth and the features in the spectrum, and provides ~30% stronger SNRs.

Each time-delay cell (baud) can be oversampled (Magri et al., 2007) to obtain sub-pixels that are correlated. The oversampling of the data reduces the thermal noise. Table 2 lists the range resolution per each range pixel and DFTs that we used to process the ranging and imaging data.

Table 1
Masterlog of Goldstone and Arecibo radar observations in 2012 and 2013.

Date	Start time (UTC) hh:mm:ss	Stop time (UTC) hh:mm:ss	Setup	Baud (μs)	spb	Code	Runs	RA (°)	Dec (°)	Distance (au)	Sol	Ptx (kW)
Goldstone												
Dec 21	10:31:49	11:53:20	Doppler	–	–	–	24	162.6	-27.3	0.103	146	430
Dec 22	10:26:51	11:23:25	Imaging	1	4	2047	17	161.4	-27.4	0.103	148	430
Jan 03	08:31:45	11:23:22	Imaging	1	4	255	53	146.4	-26.5	0.098	152	430
Jan 05	08:11:53	09:12:21	Doppler	–	–	–	19	143.6	-26.1	0.097	152	430
	09:19:14	10:00:06	Ranging	10	1	127	13					
	10:06:47	11:03:59	Imaging	1	4	255	18					
Jan 06	07:56:42	08:44:04	Imaging	1	4	255	15	142.1	-25.8	0.097	154	430
	08:50:53	11:09:53	Doppler	–	–	–	43					
Jan 08	07:36:42	11:04:13	Doppler	–	–	–	64	139.2	-25.1	0.097	156	430
Jan 09	07:21:41	08:40:52	Imaging	0.5	1	255	25	137.8	-24.7	0.097	156	430
	08:50:10	11:01:10	Doppler	–	–	–	41					
Jan 10	07:11:42	10:55:39	Imaging	0.5	4	255	68	136.3	-24.3	0.097	158	430
Jan 11	06:56:41	07:50:41	Imaging	0.5	4	255	17	134.9	-23.8	0.097	158	430
Jan 14	06:21:44	07:09:24	Imaging	1	4	255	15	130.5	-22.3	0.097	162	430
	07:18:21	10:40:10	Imaging	0.5	4	255	62					
Jan 15	06:06:45	08:44:02	Doppler	–	–	–	48	129.2	-21.7	0.098	162	430
Jan 16	05:56:44	07:07:45	Imaging	1	4	255	22	127.7	-21.1	0.098	162	430
	07:19:15	10:29:14	Imaging	–	–	–	58					
Jan 17	05:41:43	10:30:12	Doppler	–	–	–	87	126.2	-20.4	0.099	162	430
Arecibo												
Feb 18	00:46:25	01:04:43	Doppler	–	–	–	4	101.7	2.4	0.158	168	760
	01:25:27	01:49:01	Imaging	1	4	8191	5					
Feb 19	01:06:16	01:08:49	Doppler	–	–	–	1	101.5	3.0	0.161	168	720
Feb 20	00:31:11	00:44:43	Doppler	–	–	–	3	101.4	3.5	0.164	168	750
	00:48:47	02:02:27	Imaging	1	4	8191	13					
Feb 21	00:54:04	01:13:25	Doppler	–	–	–	4	101.3	4.0	0.167	168	730
Mar 15/16	22:55:56	00:57:44	Ranging	2	2	8191	16	104.0	12.7	0.236	170	740

Observations were conducted monostatically at X-band (8560 MHz, 3.5 cm, Goldstone) and S-band (2380 MHz, 12 cm, Arecibo). The times show the start and end of the reception of echoes for each setup on each day. The setups were Doppler-only CW or binary phase code imaging and ranging. For the imaging and ranging setups, we list the baud (time-delay resolution in μs), number of samples per baud (spb), and the code length "Code" which refers to the length of the repeating binary phase code. "Runs" indicates the number of transmit-receive cycles used in a specified setup. We also list right ascension, declination, distance (in au) at the start of each observing session, and the orbital solution (Sol) used to compute the delay-Doppler ephemeris predictions. The last column lists the transmitter power. At Goldstone, the electronic logs show that the transmit power remained within 1% of 430 kW. The receiver temperatures at the beginning and end of the observations were 18 ± 1 K. For Arecibo, the hand-written observation log recorded a system temperature of 27 K, except on Feb. 18 track, when there was a receiver cooling issue and the system temperatures were $40 - 50$ K at the start of the track.

2.1. First impressions of Apophis based on the radar data

Fig. 1A and B show echo power spectra at Goldstone and Arecibo. Assuming a period of ∼30 h, we averaged up to 16° of rotation in the individual spectra so that they are not significantly smeared. Table 3 lists lower bounds on echo bandwidths for each spectrum. The lower bound was estimated by counting the consecutive Doppler bins that have SNRs above 1σ and is necessarily somewhat subjective.

The minimum bandwidths at Goldstone vary by a factor of 1.75 from 0.8 Hz to 1.4 Hz. Eq. (1) shows that the Doppler bandwidth is linearly proportional to the breadth of the asteroid as it rotates. Assuming no significant changes in the sub-radar latitude from day-to-day, the dominant source for bandwidth changes are variations in the projected axes of the asteroid as it spins. The radar observations support the conclusion by Pravec et al. that Apophis is highly elongated. The narrow echo bandwidths are consistent with a slowly rotating object.

The average bandwidth measured from Arecibo echo power spectra is ∼0.4 Hz, or 1.4 Hz when converted to X-band. This corresponds to the widest bandwidths observed at Goldstone. The asteroid traversed ∼33° on the plane of sky between the last Goldstone observation on January 17 and first Arecibo observation on February 18. We would not expect a significant change in the radar-line-of-sight for this amount of the sky motion. However, the viewing geometry also changed due to Apophis' tumbling spin state, so it is possible that Arecibo observed the asteroid at different sub-radar latitude than Goldstone.

The echo power spectra in Fig. 1A and B show hints of asymmetry around zero Doppler frequency on January 5, January 17, February 18, and February 20. The shape of the echo power spectrum is closely related to the shape of the asteroid. An asymmetric echo implies that the shape of the object is asymmetric.

Fig. 2A and B show delay-Doppler images. Although the resolutions are coarse, the delay-Doppler images vary considerably in appearance and suggest an irregular shape. The echoes from January 10 and January 14 are resolved at 18.75 m/px and have a double-lobed appearance. The echoes on other days hint at an elongated shape, and a possible facet, but the images do not have sufficiently strong SNRs or resolution for reaching more definitive conclusions. Two delay-Doppler images from Arecibo in Fig. 2B have a range resolution of 37.5 m/px and very weak SNRs.

Table 3 lists lower bounds on the bandwidths and visible extents that were obtained from the images. We estimated the values from pixels 1σ above the noise level that appeared to cluster together. The longest visible extent of ∼450 m was observed on January 3, and the shortest of ∼170 m appears on January 9. If Apophis were spheroidal, then the average visible extent would provide a lower bound on the radius. Given that Apophis is elongated and possibly asymmetric, and the orientation of the spin axis plays a role in the visible extent, shape and spin models are needed to obtain an estimate of the equivalent diameter.

Table 2
Doppler-only data and delay-Doppler images used in shape modeling.

Date	Start time (UTC)	Stop time (UTC)	Runs	Setup	Resolution		Image dimensions		DFT	Looks
	hh:mm:ss	hh:mm:ss			(μs)	(Hz)	rows	columns		
Goldstone										
Dec 21	10:31:49	11:53:20	1–24	Doppler	–	0.100	–	101	500,000	307
Dec 22	10:26:51	11:23:25	1–7	Imaging	0.25	0.097	41	21	5150	289
Jan 03	08:31:45	10:11:26	1–31	Imaging	0.25	0.097	41	21	5150	527
	10:13:09	11:23:22	32–53	Imaging	0.25	0.097	41	21	5150	374
Jan 05	08:11:54	09:12:21	1–19	Doppler	–	0.100	–	101	500,000	228
	10:06:49	11:03:59	1–18	Imaging	0.25	0.097	41	21	5150	306
Jan 06	07:56:43	08:44:04	1–15	Imaging	0.25	0.097	41	21	5150	255
	08:50:54	10:01:10	1–22	Doppler	–	0.100	–	101	500,000	263
	10:02:53	11:09:53	23–43	Doppler	–	0.100	–	101	500,000	251
Jan 08	07:36:44	08:46:57	1–22	Doppler	–	0.100	–	101	500,000	264
	08:48:40	09:55:36	23–43	Doppler	–	0.100	–	101	500,000	249
	09:57:19	11:04:13	44–64	Doppler	–	0.100	–	101	500,000	253
Jan 09	07:21:42	08:40:52	1–25	Imaging	0.125	0.097	82	21	5150	375
	08:50:12	09:56:26	1–21	Doppler	–	0.100	–	101	500,000	249
	09:58:08	11:01:10	22–41	Doppler	–	0.100	–	101	500,000	236
Jan 10	07:11:43	08:51:22	1–31	Imaging	0.125	0.097	82	21	5150	527
	08:53:05	10:32:44	32–61	Imaging	0.125	0.097	82	21	5150	510
Jan 11	06:56:43	07:50:41	1–17	Imaging	0.125	0.097	82	21	5150	289
Jan 14	07:18:22	08:58:22	1–31	Imaging	0.125	0.097	82	21	5150	527
	09:00:06	10:40:10	32–62	Imaging	0.125	0.097	82	21	5150	527
Jan 15	06:06:46	06:58:05	1–16	Doppler	–	0.100	–	101	500,000	193
	06:59:49	07:51:04	17–32	Doppler	–	0.100	–	101	500,000	192
	07:52:48	08:44:02	33–48	Doppler	–	0.100	–	101	500,000	194
Jan 16	05:56:45	07:07:45	1–22	Imaging	0.25	0.097	41	21	5150	374
	07:19:17	08:23:39	1–20	Doppler	–	0.100	–	101	500,000	247
	08:25:23	09:29:45	21–40	Doppler	–	0.100	–	101	500,000	243
	09:31:30	10:29:14	41–58	Doppler	–	0.100	–	101	500,000	220
Jan 17	05:41:45	06:53:22	1–22	Doppler	–	0.100	–	101	500,000	286
	06:55:07	08:06:46	23–44	Doppler	–	0.100	–	101	500,000	270
	08:08:31	09:20:09	45–66	Doppler	–	0.100	–	101	500,000	267
	09:21:55	10:30:12	67–87	Doppler	–	0.100	–	101	500,000	273
Arecibo										
Feb 18	00:46:25	01:04:43	1–4	Doppler	–	0.050	–	120	250,000	56
	01:25:27	01:49:01	1–5	Imaging	0.25	0.050	45	41	1000	65
Feb 19	01:06:16	01:08:49	1	Doppler	–	0.050	–	120	250,000	13
Feb 20	00:31:11	00:44:43	1–3	Doppler	–	0.050	–	120	250,000	43
	00:48:47	02:02:27	1–13	Imaging	0.25	0.050	45	41	1000	169
Feb 21	00:54:04	01:13:25	1–4	Doppler	–	0.050	–	120	250,000	58

The times show the start and stop times of each shape modeling dataset. We specify which runs were summed. The data resolution is given in time delay (μs) and Doppler frequency (Hz). We also list the number of rows and columns in the Doppler-only and delay-Doppler data files. The last two columns give the length of the Discrete Fourier Transforms (DFT) and the number of looks (the number of statistically independent measurements), for each data file. The last delay-Doppler echo from March 15 had coarse resolution and SNRs that were too low to be useful with shape modeling.

Nevertheless, the images place a lower bound on the long axis of 450 m.

3. Size, spin, and shape constraints based on the radar data

The radar data are not strong enough for 3D shape modeling, nor do they provide sufficient rotational coverage, so we adopted the Pravec et al. shape and spin state to check for consistency and to see if we could improve them. We expected the radar data to be sufficient for Apophis' equivalent diameter estimate, a parameter that cannot be determined from the lightcurves. In this section we describe the subset of the radar data we used (Section 3.1) and we also give an overview of the 3D modeling process (Section 3.2).

We started with fixed Pravec et al. spin state and shape, and calculated χ^2 with respect to 16 values for the equivalent diameter. Then we used scaled models, held at fixed values, and explored the parameter space of possible spin states to see if we could improve the fits. Finally, we attempted to fit the bifurcation visible in the images to the shape. For this last approach, we started with either the Pravec et al. convex model or two ellipsoids in contact and allowed shape and spin parameters to float. In summary, Section 3.3 discusses Apophis' size estimate, Section 3.4 investigates the spin state, and Section 3.5 offers possible improvements to shape of Apophis based on the radar data.

3.1. Shape modeling data set

Table 2 summarizes the shape modeling data set, which consists of 23 echo power spectra and 14 delay-Doppler images covering 17 days from December 21 to February 21. Each image or spectrum contains between 14 min and 1.7 h of integration time. We incoherently summed as many runs as possible in order to maximize the SNRs while simultaneously keeping the rotational smear to less than 20°. We used masking frames to isolate the echo and to reduce the number of degrees of freedom in the fit. This was critical to get the reduced χ^2 to be around or above unity.

The data weights were balanced so the echo power spectra and the delay-Doppler images contributed roughly the same number of degrees of freedom (4476 and 4356 respectively) to the overall χ^2. Although we investigated alternative weights, the nominal approach provided a balance between the more abundant echo power spectra and size-constraining delay-Doppler images.

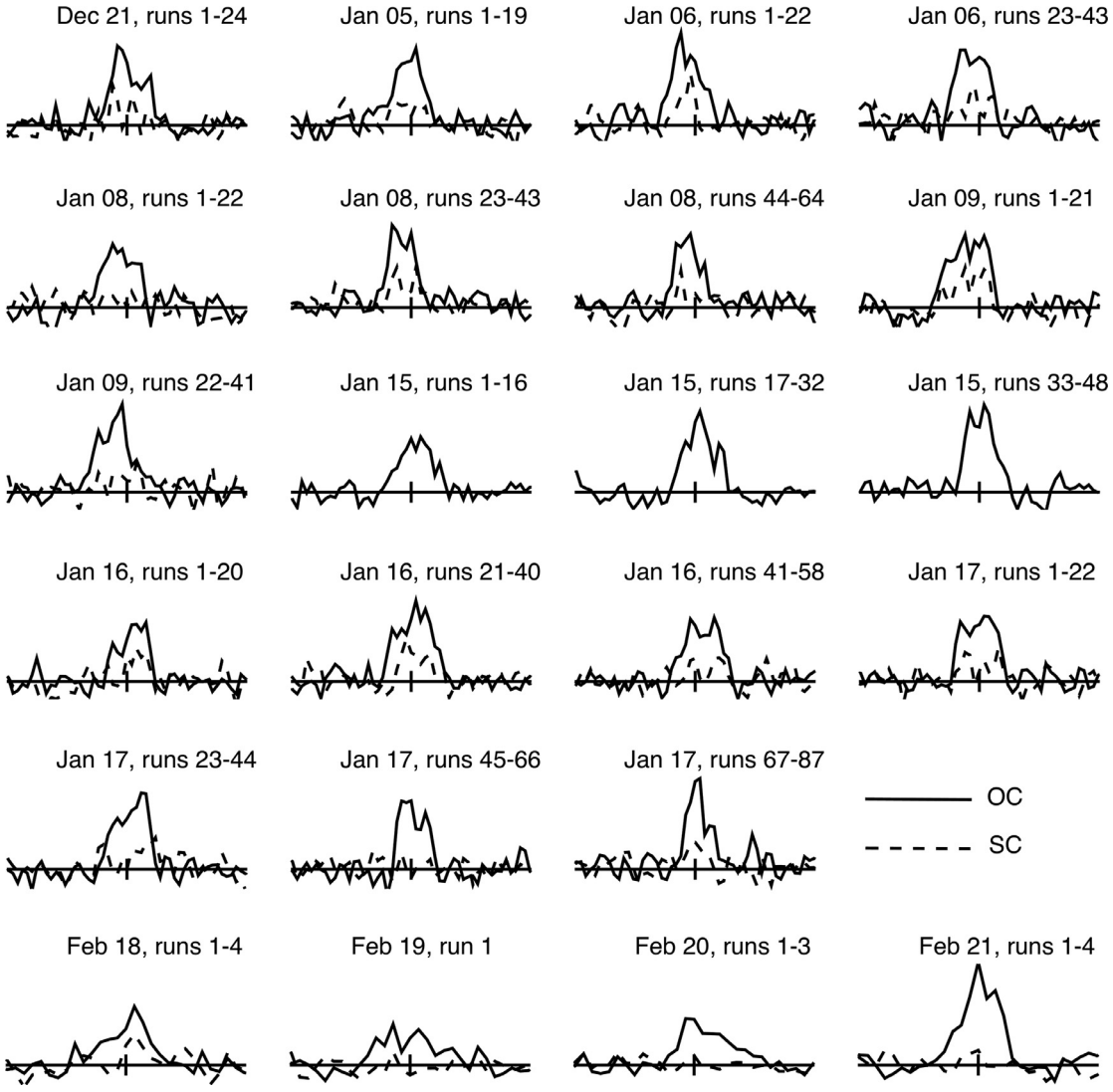

Fig. 1. A. OC (solid line) and SC (dashed line) echo power spectra from December 21, 2012 to January 17, 2013 obtained at Goldstone (X-band). On January 15 only OC data were recorded. Labels contain run numbers that were summed to make each spectrum. Table 2 lists the start-stop times and the number of looks for these sums. Each spectrum is centered at 0 Hz and extends from −2.5 Hz to +2.5 Hz with a frequency resolution of 0.1 Hz. All spectra were normalized to have zero mean and unit standard deviation of the receiver noise. The vertical tick at 0 Hz shows ±1 standard deviation. Identical linear scales are used for all spectra. B. Echo power spectra from February 18 to 21, 2013 obtained at Arecibo. Each spectrum extends from −0.7 Hz to +0.7 Hz with a frequency resolution of 0.05 Hz.

3.2. Shape modeling process

The *Shape* software (Hudson 1994, and Magri et al., 2007) uses a constrained, weighted least-squares minimization procedure to find the best set of parameters that model the shape, spin state, and radar scattering law. The algorithm adjusts one parameter at a time, which ignores correlations, and can lead to a solution that corresponds to a local minimum in the χ^2 space. Ideally, the user explores the parameter space by keeping most of the values fixed in a systematic grid, while allowing a small number of parameters to adjust. For Apophis, we hard-wired the shape, size, and spin parameters for a given modeling run. This was a conservative approach adopted so that *Shape* would not get stuck at the local minimum. The only parameters that were free to adjust were coefficients of the 1st order polynomials ("delcor" coefficients) that correct the ephemeris delay and Doppler predictions as a function of time. By varying these coefficients, *Shape* shifts the synthetic echo in delay-Doppler space, looking to minimize χ^2 by finding the optimal overlap between the radar data and the synthetic echo.

3.3. Size constraints

In this section we adopt the Pravec et al. model and scale its equivalent diameter, a diameter that a sphere with the same volume as the shape model would have, to a range of values in an attempt to find the best fit for the size of Apophis. The Pravec et al. (2014) shape model is defined by 1014 vertices and 2024 facets. The mean edge length is ∼25 m, which is comparable to the highest resolution in the delay-Doppler data. We used a single parameter to scale the size of the Pravec et al. shape model. We considered 16 scales that produced equivalent diameters between 0.25 km and 0.40 km in steps of 0.01 km. These sizes cover the diameters of Apophis reported by Delbo et al. (2007), Müller et al. (2014), and Licandro et al. (2016).

Fig. 3 shows reduced χ^2 values for the 16 different equivalent diameters. Our data set has a total number of degrees of freedom $N = 8832$. The minimum χ^2 was achieved for an equivalent diameter of 0.34 km. The upper and lower 1σ bounds can be estimated if we draw a line at $\chi^2_{min} + \frac{\sqrt{2N}}{N}\chi^2_{min}$ (for a review of χ^2 distri-

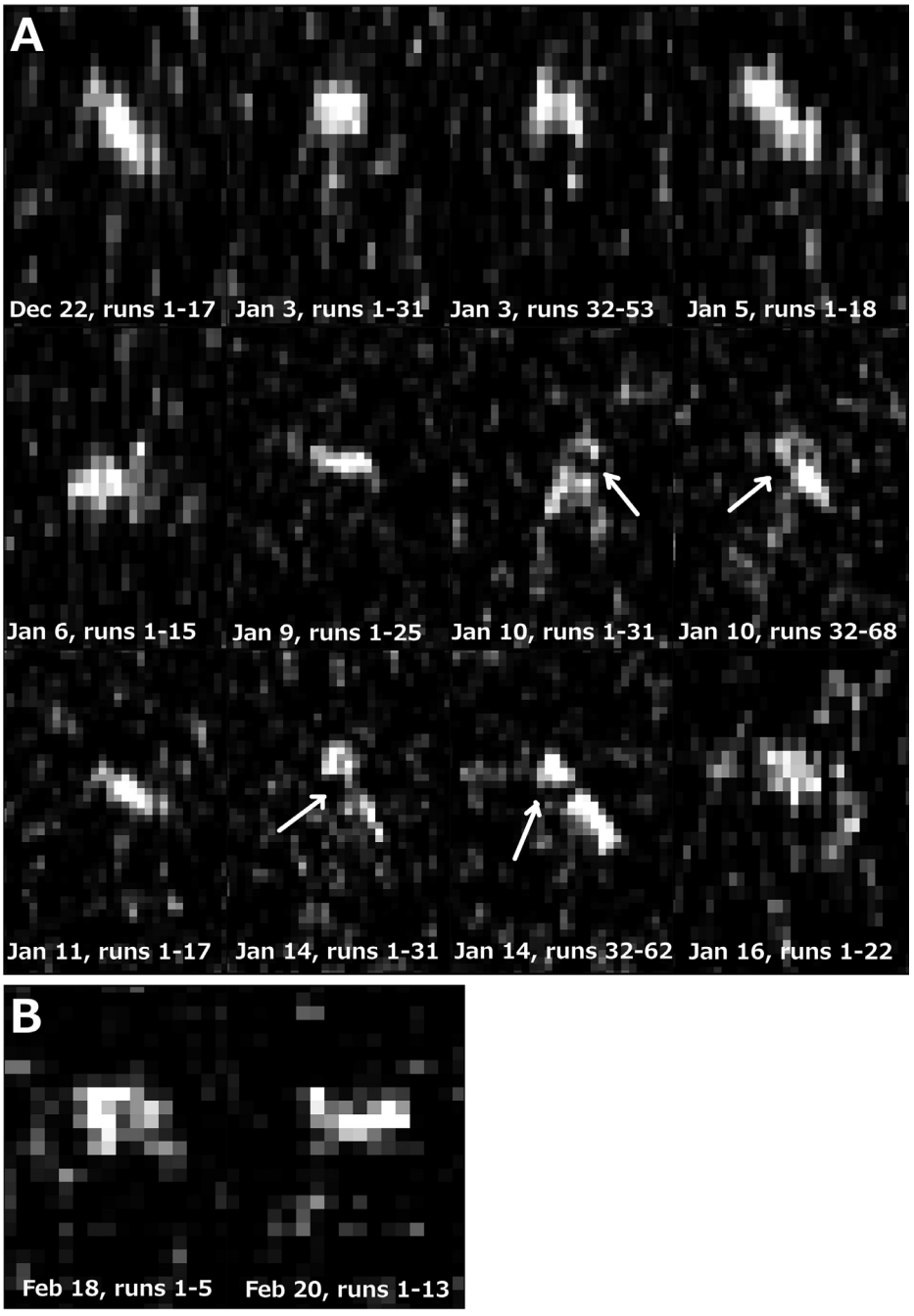

Fig. 2. A. Delay-Doppler images from December 22 to January 16 obtained at Goldstone. Time delay (range) increases from top to bottom and Doppler frequency increases from left to right. The vertical dimension of each image is 0.9 km and the horizontal dimension is 3 Hz. The delay-Doppler data were normalized so that the noise has zero mean and unit standard deviation. Labels contain run numbers, or indexed transmit and receive cycles, that were summed. Table 2 lists start-stop times and the number of looks. White arrows point to features that may be a bifurcation in the echoes. B. Delay-Doppler images from February 18 and 20 obtained at Arecibo. The vertical dimension of each panel is 0.9 km and the horizontal dimension is 0.83 Hz, chosen so the width of the images, if converted to X-band, is the same as the Goldstone images.

bution properties, see Hogg and Tanis, 1993). Taken at face value, Fig. 3 gives the best fit of $D = 0.340^{+0.015}_{-0.035}$ km (1σ bounds).

Our nominal equivalent diameter of 0.34 km is smaller than the most recent thermal modeling estimate of 0.380 – 0.393 km by Licandro et al. (2016). Figs. 4 and 5 show how synthetic echo power spectra and delay-Doppler images generated from the Pravec et al. model scaled to 0.34 km (our nominal diameter) and 0.38 km (Licandro et al. lower bound) compare with the radar data. The fits to the Doppler-only data appear nearly identical for both sizes (Fig. 4). This is not surprising given that they are only coarsely resolved. The majority of the fit sensitivity comes from the delay-Doppler images because they constrain the visible extent at the level of the range resolution (Fig. 5). Most of the delay-Doppler images have effective resolutions of 18.75 m and 37.5 m. The reduced χ^2 values are 1.443 for $D = 0.34$ km and 1.541 for $D = 0.38$ km. Fig. 3 shows that statistically, an equivalent diameter of $D = 0.38$ km gives a fit that is $> 3\sigma$ worse than the fit obtained with $D = 0.34$ km. Visually, the difference is subtle, so we adopted $D = 0.38$ km is a conservative 1σ upper bound on the equivalent diameter.

Fig. 3 implies that the 3σ lower bound on the equivalent diameter is ~0.27 km, which matches the diameter of 0.27 ± 0.06 km re-

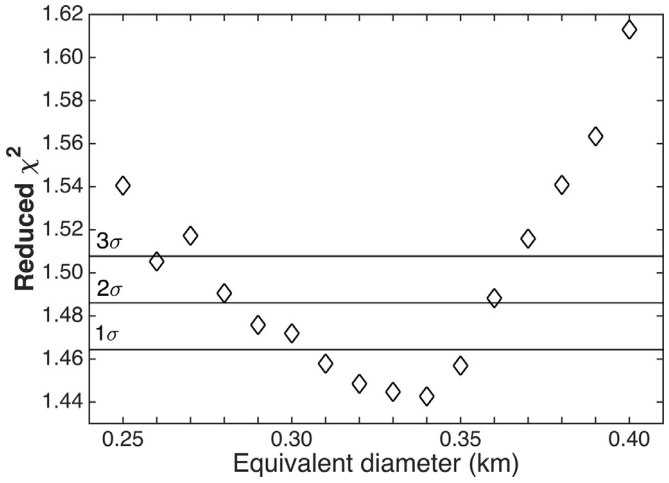

Fig. 3. Reduced χ^2 values for a range of equivalent diameters using the shape and spin model from Pravec et al. (2014). The reduced χ^2 scores represent fits to the radar data shown in Figs. 1 and 2 where the equivalent diameter was scaled between 0.25 and 0.40 km. Horizontal lines mark 1σ, 2σ, and 3σ bounds calculated from the minimum reduced χ^2 and the number of degrees of freedom.

ported by Delbo et al. (2007). The visible extent appears too short below an equivalent diameter of 0.30 km (Supplementary Fig. 1), but this may be a subjective judgment. Based on Fig. 4 and our visual inspection, we adopt equivalent diameter for Apophis to be $D = 0.34 \pm 0.04$ km (1σ). For comparison, much stronger radar data sets such as (214869) 2007 PA8 (Brozovic et al., 2017) allow estimates an equivalent diameter on the order of 5%.

3.4. Spin state constraints

Our second objective was to test if the radar data allow us to improve estimates of the spin state. We adopted the Pravec et al. 3D model, scaled it to 16 equivalent diameters between 0.25 and 0.40 km, and paired these with 3000 variants of the spin state based on Table 2 in Pravec et al. We found these variants by randomly sampling hundreds of thousands of Euler angles, spin rates, and moments of inertia values, and by keeping the combinations that met the Pravec et al. criteria. Supplementary Figs. 2A and 2B show projections of the eight-parameter NPA spin state space generated for this experiment. The distribution of admissible angular momentum vectors in ecliptic longitude (λ) and latitude (β) closely reproduces the distribution in Fig. 3 in Pravec et al.

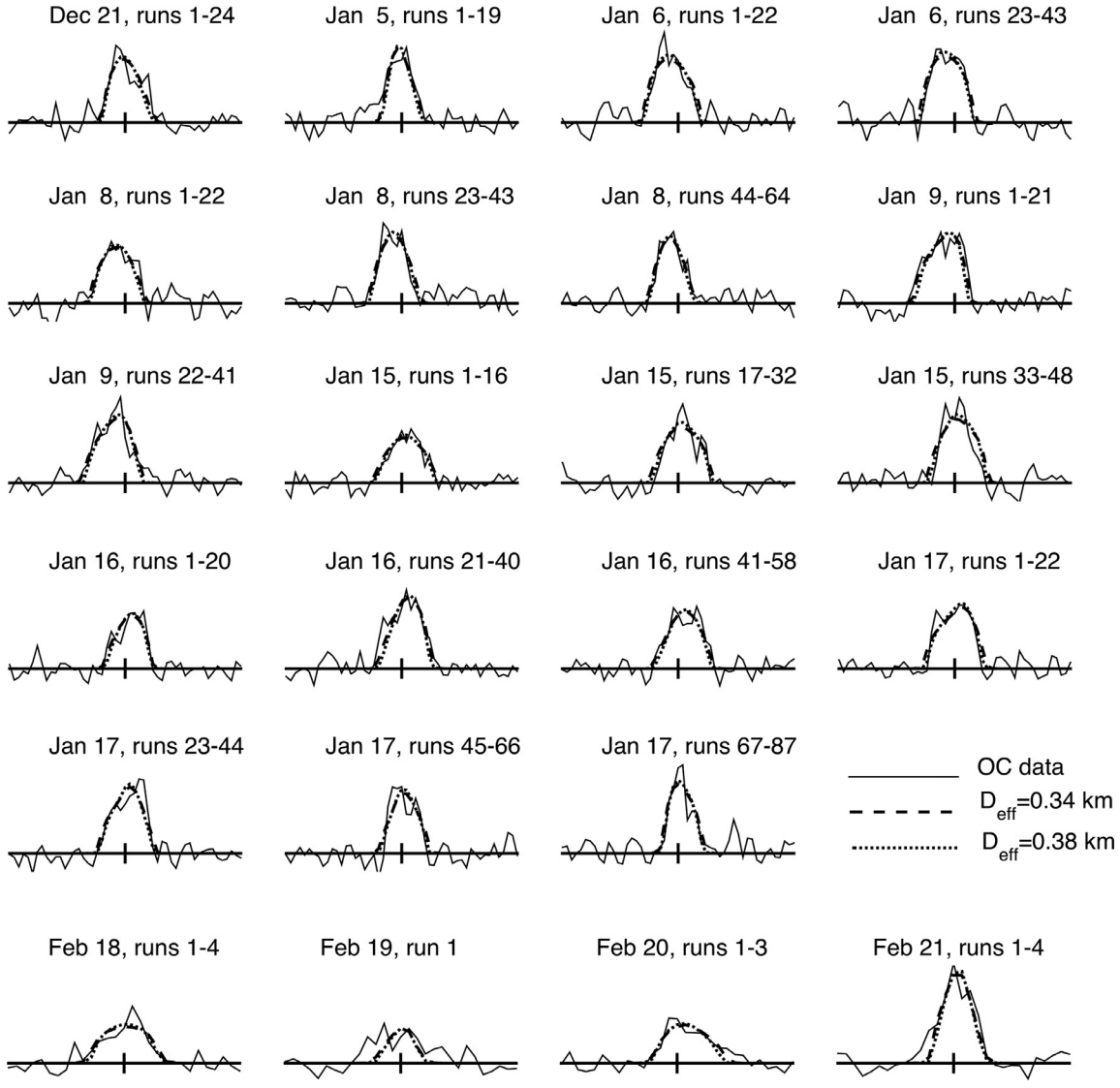

Fig. 4. OC data fits based on the shape and spin model from Pravec et al. The shape models are scaled to equivalent diameters of D = 0.34 km (grey solid line) and D = 0.38 km (black dashed line). Fits using different diameters are nearly indistinguishable. OC echo power spectra are shown as thin black lines. A. Goldstone data. B. Arecibo data.

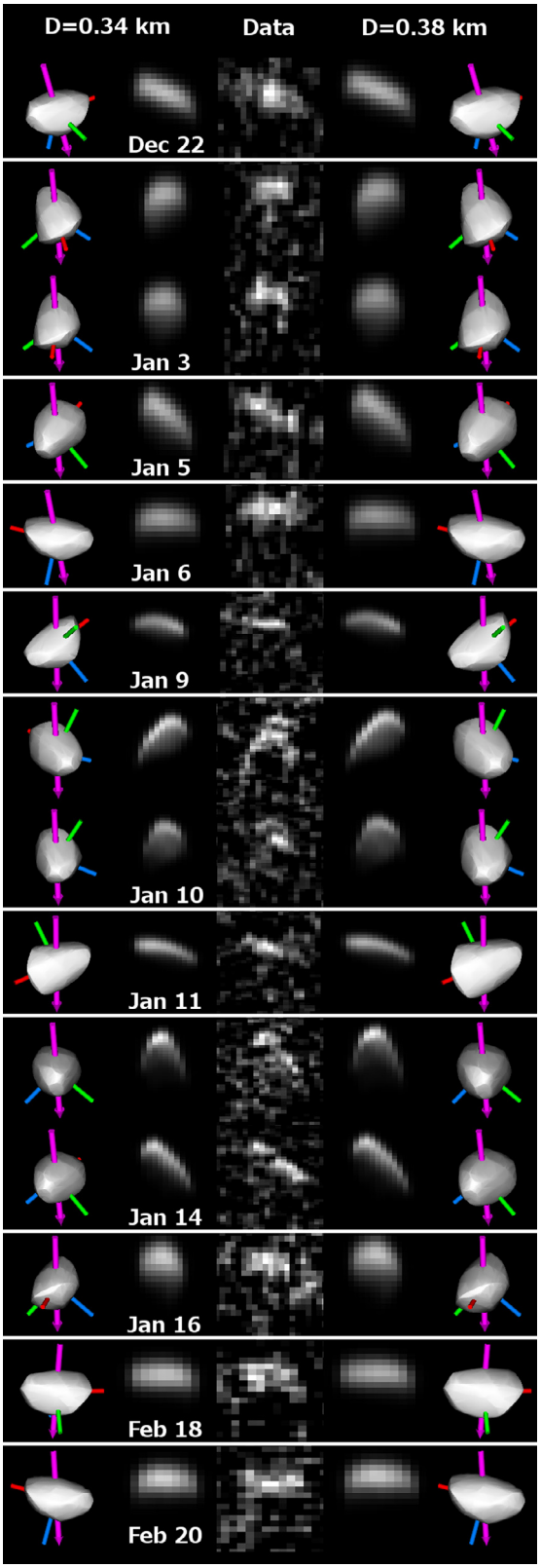

Fig. 5. Collage of, from left to right: plane-of-sky renderings of the Pravec et al. model scaled to D = 0.34 km, corresponding fits (synthetic images), delay-Doppler radar images, fits produced by a model scaled to D = 0.38 km, and corresponding plane-of-sky renderings for the larger shape model. In the data and fits, time delay increases from top to bottom, and Doppler frequency increases from left to right. The plane of sky view is contained in a 0.7 km × 0.7 km square with 151 × 151 pixels. The magenta arrow shows the instantaneous orientation of the spin vector, and the red, green, and blue shafts denote the positive ends of the long, intermediate, and short principal axes. (For interpretation of the references to colour in this figure legend, the reader is referred to the web version of this article.)

Table 3
Echo bandwidths and visible range extents.

Date	Bandwidth (Hz)	Visible extent (m)
Goldstone	**X-band**	
Dec 21	1.0	–
Dec 22	1.2	412.5
Jan 3	0.9	450.0
	1.0	450.0
Jan 5	1.3	–
	1.2	337.5
Jan 6	1.3	300.0
	1.1	–
	1.0	–
Jan 8	1.0	–
	1.0	–
	0.9	–
Jan 9	0.9	168.75
	1.2	–
	1.4	–
Jan 10	0.9	431.25
	0.9	356.25
Jan 11	1.1	206.25
Jan 14	0.8	300.0
	1.1	300.0
Jan 15	1.2	–
	1.0	–
	1.0	–
Jan 16	0.9	225.0
	0.9	–
	1.2	–
	1.2	–
Jan 17	1.0	–
	1.0	–
	0.8	–
	0.8	–
	1.04 ± 0.16	328.1 ± 96.1
Arecibo	**S-band**	
Feb 18	0.40	–
	0.40	262.5
Feb 19	0.40	–
Feb 20	0.45	–
	0.40	187.5
Feb 21	0.35	–
	0.40 ± 0.03	225.0 ± 53.0

Lower bounds on echo bandwidths and visible extents estimated from the echo power spectra and radar images shown in Figs. 1 and 2. The measurements count the points (echo power spectra) or pixels (images) that are at least 1σ above the noise level and are adjacent to other points or pixels considered to be a part of the echo. Doppler resolution is 0.10 Hz for Goldstone data and 0.05 Hz for Arecibo data. Range resolution is 37.5 m on December 22, January 3, 5, 6, 16, February 18 and 20, and 18.75 m on January 9, 10, 11, and 14. There are no errors associated with the individual measurements because these are lower bounds.

We selected the size that minimizes χ^2 for each of the candidate spin states. The vertex models were kept fixed. We obtained the best χ^2 for the spin state that has an angular momentum vector pointing at $\lambda = 246.8°$ and $\beta = -59.3°$. The comparison of this and Pravec et al. (2014) angular momentum vector is shown in Supplementary Fig. 2A. We designate this as Model R, for "radar-selected", and the full spin state is listed in Supplementary Table 1. Model R has reduced $\chi^2 = 1.398$ for $N = 8332$. A visual comparison between Model R (Supplementary Fig. 3) and the Pravec et al. model (Fig. 5) reveals that the leading edges on January 10 and 14 appear to be better aligned with the data using Model R. However, the radar data are weak enough that this is probably not the "true" spin state of Apophis, but just one of the variants allowed by the uncertainties.

3.5. Shape constraints

Our next goal was to test if the radar data can improve shape fits to the bifurcated echoes observed on January 10 and 14. We

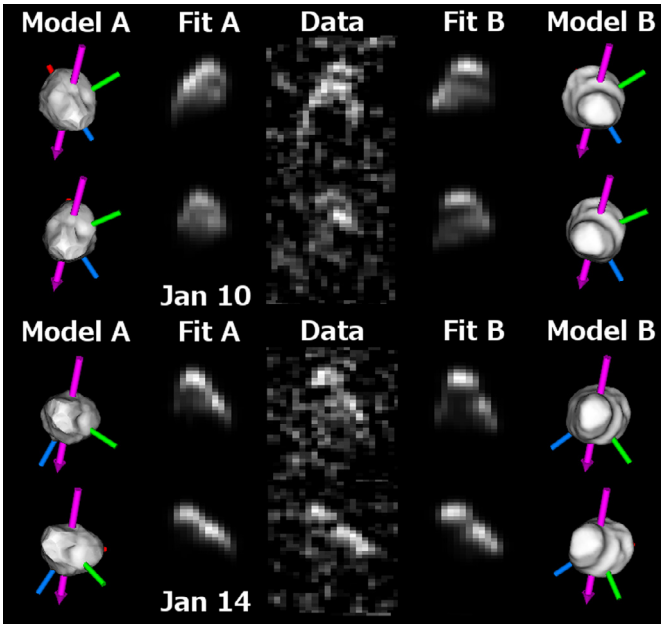

Fig. 6. Data, fits, and 3D models for two vertex models that are bifurcated. Collage of, from left to right: plane-of-sky renderings of Model A and its corresponding fits, delay-Doppler radar images, fits and plane-of-sky views of Model B. For additional description, see caption of Fig. 5. Fits to other radar images not shown here appear in Supplementary Fig. 4.

tried two strategies: Model A used the Pravec et al. 3D model as the starting point, and Model B started with two ellipsoids in contact. All parameters including the spin state were allowed to adjust during the fit. Model B went through two levels of shape refinement, first as a 10-th order spherical harmonics model, and second as the vertex model realized with 2000 vertices and 3996 facets. This gives the same spatial resolution as Model A.

Fig. 6A and B show fits to delay-Doppler images from January 10 and 14 for Model A, Model B, and Supplementary Fig. 4 shows fits to the rest of the data. Model A developed a "pinch" on the narrow end that results in better correspondence between the data and the fits on January 10 and 14. Model B shows that the delay-Doppler data can tolerate an even more dramatic bi-lobed appearance. Visually, Model B fits the data better although the χ^2 for both models are within 1σ and are statistically indistinguishable. Both models fit the data better than Pravec et al. model with no bifurcation. We conclude that the radar data suggest that Apophis is at least somewhat bifurcated.

4. Disk-integrated properties

Table 4 lists disk-integrated properties for Apophis. The mean Goldstone OC cross-section, calculated as an unweighted mean of daily averages, is $\sigma_{OC} = 0.023 \pm 0.008$ km^2. We assigned a 35% error in order to account for systematic calibration and pointing errors. The Arecibo cross-section estimate of $\sigma_{OC} = 0.016 \pm 0.006$ km^2 is based on four echo power spectra obtained on February 18–21. Three of these spectra have SNRs of only ~5. The lowest daily average OC cross-section at Goldstone is 0.020 km^2 and the highest is 0.029 km^2, a 45% difference that is not surprising given the elongated shape.

Within the error bars, our results are consistent with the cross-section $\sigma_{OC} = 0.019 \pm 0.009$ km^2 reported by Giorgini et al. (2008). The previous result was based on three low-SNR echo power spectra obtained at Arecibo in 2005. The 2005 cross-sections varied by a factor of two which now are understandable due to the elongated shape.

Table 4 lists the circular polarization ratio, SC/OC, for each spectrum. The values show large variations from day-to-day and on individual days because the SNRs for the SC echoes are low. The mean value and standard deviation is 0.33 ± 0.11 for data obtained at Goldstone. We used daily averages to calculate the overall mean. The SC echoes at Arecibo were too weak to make a meaningful estimate. Our X-band circular polarization ratio is consistent with results found for 70 S-class NEAs by Benner et al. (2008), who reported a mean SC/OC $= 0.27 \pm 0.08$.

The SC/OC ratio for Apophis is comparable to 3.5-cm wavelength values seen for (4179) Toutatis, 0.29 ± 0.01 (Ostro et al., 1999), (433) Eros, 0.33 ± 0.07 (Magri et al., 2001), and (4) Vesta, 0.32 ± 0.04 (Mitchell et al., 1996) suggesting similar near-surface structural complexity. Toutatis and Eros are both S-class objects, which makes them comparable to Apophis' Sq class taxonomy. The ratio for Apophis is larger than that estimated for (101955) Bennu, 0.14 ± 0.03 (Nolan et al., 2013), suggesting a rougher surface at decimeter spatial scales. Bennu is a C-class object.

The mean OC radar albedo was calculated by dividing the measured OC cross-section by the projected area of a sphere with an equivalent diameter D. This approach assumes that we have sampled the rotation of Apophis well enough that we do not have a bias in the mean OC cross-section estimate. Given that we have reasonable rotation coverage at Goldstone and four consecutive days sampled at Arecibo, the error due to sampling should be covered with our fairly conservative 35% error on the cross-section. If we adopt $\sigma_{OC} = 0.023 \pm 0.008$ km^2 for the Goldstone cross-section, D $= 0.34 \pm 0.04$ km, and propagate the errors, then we obtain mean $\eta_{OC} = 0.25 \pm 0.11$. For Arecibo data, we obtain mean $\eta_{OC} = 0.18 \pm 0.08$. These results are consistent with each other and with the day-to-day variations in the radar albedo estimates. The OC Goldstone radar albedo and the standard deviation from daily averages is 0.24 ± 0.03, and the OC albedo from daily values at Arecibo is 0.19 ± 0.10.

The average OC albedo calculated from 21 S-class NEAs that have been observed by radar and that have an estimate of the size is $\eta_{OC} = 0.15 \pm 0.06$, https://echo.jpl.nasa.gov/~lance/asteroid_radar_properties/nea.radaralbedo.html. We conclude that Apophis has a slightly higher radar albedo than the average seen among S-class NEAs. For comparison, the radar albedos of three NEAs visited by spacecraft are 0.25 ± 0.09 for Eros (Magri et al., 2001), 0.21 ± 0.03 for Toutatis (Ostro et al., 1999), and 0.21 ± 0.05 for Itokawa. We updated the radar estimate for Itokawa based on the Arecibo OC cross-sections (Ostro et al., 2004) and an equivalent diameter of 0.33 ± 0.02 km measured by the Hayabusa spacecraft (Demura et al., 2006).

5. Optical albedo

We estimate the visual geometric albedo from the equivalent diameter D $= 0.34 \pm 0.04$ km result (Section 3.3) and the absolute visual magnitude of $H_V = 19.09 \pm 0.19$ from Pravec et al. (2014). The optical albedo was calculated using the expression $p_V = (1329/D)^2 \times 10^{-0.4Hv}$ (Pravec and Harris, 2007) and we obtain $p_V = 0.35 \pm 0.10$. For comparison, Licandro et al. (2016) reported p_V for Apophis in the range of 0.24–0.33, which is still within our bounds.

Apophis was classified as an Sq object (Binzel et al., 2009) in Bus-DeMeo taxonomy, and Mainzer et al. (2011) reported an average optical albedo of 0.24 ± 0.04 for 6 Bus-DeMeo Sq taxonomy asteroids (3 NEAs and 3 main belt) based on the fully cryogenic portion of the NEOWISE mission. On a broader scale, Thomas et al. (2011) estimated $p_V = 0.24 \pm 0.04$ as the mean optical albedo for 46 objects from Spitzer ExploreNEOs survey that were classified as S type in the Tholen-Bus-Bus-DeMeo taxonomy. Furthermore, the 40 NEOs in the Tholen-Bus-Bus-DeMeo

Table 4
Disk-integrated properties.

Date	Start time (UTC) hh:mm:ss	Stop time (UTC) hh:mm:ss	Runs	looks	OC SNRs	σ_{OC} (km^2)	SC/OC	Area (km^2)	η_{OC}
Goldstone									
Dec. 21	10:31:49	11:53:20	1–24	568	7.9	0.023	0.17	0.098	0.234
Jan. 5	08:11:54	09:12:21	1–19	424	9.0	0.022	0.53	0.093	0.234
Jan. 6	08:50:54	10:01:10	1–22	490	10.6	0.027	0.31	0.101	0.269
Jan. 6	10:02:53	11:09:53	23–43	469	14.2	0.030	0.27	0.099	0.303
Jan. 8	07:36:44	08:46:57	1–22	494	9.2	0.022	0.18	0.095	0.229
Jan. 8	08:48:40	09:55:36	23–43	465	8.0	0.021	0.51	0.090	0.232
Jan. 8	09:57:19	11:04:13	44–64	477	9.5	0.016	0.35	0.086	0.185
Jan. 9	08:50:12	09:56:26	1–21	462	10.8	0.031	0.30	0.098	0.316
Jan. 9	09:58:08	11:01:10	22–41	440	10.0	0.027	0.31	0.102	0.267
Jan. 15	06:06:46	06:58:05	1–16	360	6.3	0.020	–	0.102	0.195
Jan. 15	06:59:49	07:51:04	17–32	360	9.4	0.022	–	0.102	0.212
Jan. 15	07:52:48	08:44:02	33–48	360	10.1	0.022	–	0.100	0.216
Jan. 16	07:19:17	08:23:39	1–20	452	8.5	0.015	0.45	0.087	0.175
Jan. 16	08:25:23	09:29:45	21–40	452	8.4	0.022	0.29	0.093	0.237
Jan. 16	09:31:30	10:29:14	41–58	410	9.7	0.023	0.12	0.097	0.236
Jan. 17	05:41:45	06:53:22	1–22	504	8.9	0.021	0.24	0.104	0.198
Jan. 17	06:55:07	08:06:46	23–44	501	11.0	0.020	0.46	0.098	0.209
Jan. 17	08:08:31	09:20:09	45–66	504	11.4	0.016	0.57	0.091	0.181
Jan. 17	09:21:55	10:30:12	67–87	471	10.7	0.022	0.16	0.083	0.261
Arecibo									
Feb. 18	00:46:25	01:04:43	1–4	60	5.3	0.015	–	0.111	0.139
Feb. 19	01:06:16	01:08:49	1	15	5.3	0.025	–	0.076	0.324
Feb. 20	00:31:11	00:44:43	1–3	46	4.6	0.009	–	0.103	0.086
Feb. 21	00:54:04	01:13:25	1–4	63	10.3	0.016	–	0.078	0.201

Disk-integrated radar properties of Apophis. σ_{OC} is the OC radar cross-section and SC/OC is circular polarization ratio estimated from the echo power spectra in Fig. 1. SC/OC ratios were calculated from data processed at 0.25 Hz resolution (Goldstone) and 0.1 Hz resolution (Arecibo). Resolutions were chosen in order to provide enough looks to obtain Gaussian noise statistics and to show clear echoes. The number of looks represents the number of statistically independent measurements. We also list the run numbers that were summed and the SNRs in OC echo power spectra. The SNRs for the SC spectra at Goldstone were between 1.7 and 4.4. OC radar albedo (η_{OC}) is calculated by dividing the radar cross-section (σ_{OC}) by the model's projected surface area. The projected surface area was calculated from the Pravec et al. model scaled to D = 0.34 km.

Q taxonomy have an average optical albedo of $p_V = 0.25 \pm 0.06$. Pravec et al. (2012) revised optical albedo values estimated by the NEOWISE by de-biasing the absolute magnitudes. Pravec et al. found that the mean albedo of S, A, and L types with sizes 0.6–200 km is $p_V = 0.20 \pm 0.05$.

Our result implies that Apophis could be on the optically brighter end of the Sq taxonomy, although the statistics for this group is still based on a small number of NEAs. Furthermore, this results hinges on the Pravec et al. estimate of $H_V = 19.09 \pm 0.19$ that changed by more than 1σ from Delbo et al. (2007), $H_V = 19.7 \pm 0.4$.

6. Orbital fit

Giorgini et al. (2008) reported an orbital fit to all astrometry available for Apophis through mid-2006. Here we examine updated orbit solutions that extend the data arc nine years to 2015, use six times as much optical astrometry, and include newly reduced radar astrometry from 2012 to 2013. We excluded 19 optical measurements found to be gross outliers. The nominal optical data weights were assigned as in Vereš et al. (2017) although we further deweighted a number of measurements to allow for localized short-term systematic site biases evident upon inspection.

We used Model R (Supplementary Fig. 3) for high-precision *Shape*-based center-of-mass (COM) radar astrometry to replace visually estimated COM measurements initially reported during the radar observations in 2013. We chose Model R because it showed good agreement between the data and the fits. The two scaled Pravec et al. models from Fig. 5 and Model A from Fig. 6 were used as a cross check for the COM location. All models give COM estimates within the same delay and Doppler bins. Table 5 lists 11 time-delay and 23 Doppler *Shape*-based radar astrometry measurements. The uncertainties were assigned to be up to two delay or Doppler resolution bins, depending on our subjective assessment of the echo quality. We also kept three visually estimated time-delay measurements from January 3, 5, and 16 as a consistency check of the new astrometry, and the March 15 Arecibo ranging measurement which extended the data arc by more than three weeks.

Previous work by Giorgini et al. (2008), Farnocchia et al. (2013), and Vokrouhlický et al. (2015) showed that the Yarkovsky effect is the dominant source of the uncertainties for the orbit of Apophis. Vokrouhlický et al. (2015) used the early radar measurements reported in 2013 and optical data through February 2014 in their orbital fit and they concluded that the existing optical and radar data show no evidence for the Yarkovsky acceleration. In order to predict possible offsets from the ballistic trajectory and to obtain more realistic orbital uncertainty estimates due to the Yarkovsky effect, their orbital fits implemented a theoretical model for the Yarkovsky effect with plausible assumptions about the asteroid's spin state, size, surface density, and thermal conductivity. Vokrouhlický et al. (2015) reported that the inclusion of the Yarkovsky effect shifts the orbit of Apophis by several hundred km with respect to a purely ballistic trajectory during the 2029 approach and that the orbital uncertainties grow by an order of magnitude, from 6 km to 90 km.

Our current dynamical model addresses many systematic deficiencies explored for solution 142 by Giorgini et al. (2008); we use the modern DE431 planetary ephemeris perturbers instead of DE405, an Earth J_2 oblateness model instead of a point-mass acceleration, and sixteen asteroid perturbers instead of three. All trajectories result from numerically integrated parameterized post-Newtonian (PPN) equations of motion. The trajectory uncertainties

Table 5
Apophis radar astrometry.

UTC epoch of the echo reception	Obs.	Time delay estimate (s)	err. (μs)	resid. (μs)	Nresid.	Doppler freq. estimate (Hz)	err. (Hz)	resid. (Hz)	Nresid.
2005 01 27 23:31:00	A	–				−100,849.143	0.250	−0.049	0.196
2005 01 29 00:00:00	A	192.02850713	4.000	0.273	0.068	−102,512.906	0.250	0.017	0.066
2005 01 30 00:18:00	A	195.80817079	4.500	0.313	0.070	−103,799.818	0.150	0.058	0.386
2005 08 07 17:07:00	A	–				8186.800	0.200	−0.098	0.491
2006 05 06 12:49:00	A	–				−118,256.800	0.100	−0.006	0.065
2012 12 21 11:10:00	**G**	**–**				**57,992.443**	**0.250**	**0.039**	**0.155**
2012 12 22 11:00:00	**G**	**102.68298605**	**0.250**	**0.105**	**0.422**	**57,880.250**	**0.100**	**−0.023**	**0.234**
2013 01 03 09:20:00	**G**	**97.44910761**	**0.250**	**0.023**	**0.090**	**36,629.285**	**0.100**	**−0.001**	**0.011**
2013 01 03 10:00:00	G	97.43930871	3.000	−0.491	0.164	–			
2013 01 03 10:50:00	**G**	**97.42842546**	**0.250**	**0.018**	**0.073**	**–**			
2013 01 05 08:40:00	**G**	**–**				**30,404.009**	**0.200**	**0.107**	**0.534**
2013 01 05 10:40:00	**G**	**96.91159152**	**0.250**	**−0.123**	**0.494**	**20,031.160**	**0.100**	**−0.061**	**0.609**
2013 01 05 10:50:00	G	96.91021803	3.000	−0.599	0.200	–			
2013 01 06 08:20:00	**G**	**–**				**26,660.815**	**0.100**	**−0.052**	**0.520**
2013 01 06 09:30:00	**G**	**–**				**20,775.144**	**0.100**	**0.037**	**0.370**
2013 01 08 08:10:00	**G**	**–**				**15,496.441**	**0.100**	**−0.009**	**0.092**
2013 01 09 08:00:00	**G**	**96.45144973**	**0.200**	**0.121**	**0.606**	**9670.119**	**0.100**	**−0.007**	**0.075**
2013 01 09 09:20:00	**G**	**–**				**2690.401**	**0.100**	**−0.027**	**0.266**
2013 01 10 08:00:00	**G**	**96.47265272**	**0.200**	**0.072**	**0.362**	**2590.857**	**0.100**	**0.031**	**0.309**
2013 01 10 09:40:00	**G**	**96.47392480**	**0.200**	**0.056**	**0.280**	**–**			
2013 01 11 07:20:00	**G**	**–**				**−1589.599**	**0.200**	**0.113**	**0.565**
2013 01 14 08:10:00	**G**	**97.25834356**	**0.200**	**0.021**	**0.104**	**−30,561.776**	**0.100**	**−0.062**	**0.624**
2013 01 14 09:50:00	**G**	**97.28303717**	**0.200**	**0.059**	**0.297**	**–**			
2013 01 15 06:30:00	**G**	**–**				**−30,666.291**	**0.100**	**0.010**	**0.099**
2013 01 16 06:30:00	G	98.086754	1.000	−0.374	0.374	**−39,582.277**	**0.200**	**−0.077**	**0.384**
2013 01 16 07:50:00	**G**	**–**				**−46,641.384**	**0.100**	**0.070**	**0.704**
2013 01 17 06:20:00	**G**	**–**				**−47,875.142**	**0.100**	**−0.006**	**0.058**
2013 02 18 00:56:00	**A**	**–**				**−76,760.475**	**0.200**	**0.009**	**0.045**
2013 02 18 01:37:00	**A**	**157.90644415**	**0.250**	**−0.154**	**0.614**	**−78,041.365**	**0.200**	**−0.068**	**0.340**
2013 02 19 01:08:00	**A**	**–**				**−78,105.657**	**0.200**	**0.004**	**0.020**
2013 02 20 00:38:00	**A**	**–**				**−78,070.341**	**0.200**	**0.023**	**0.115**
2013 02 20 01:26:00	**A**	**163.57887587**	**0.250**	**0.049**	**0.198**	**−79,560.965**	**0.200**	**0.016**	**0.078**
2013 02 21 01:04:00	**A**	**–**				**−79,697.130**	**0.200**	**0.029**	**0.144**
2013 03 15 23:59:00	A	235.22085507	2.000	0.400	0.200	−80,977.525	0.238	0.150	0.631

Entries report the measured round-trip delay time in μs and Doppler frequency-shift in Hz for echoes relative to Apophis estimated center-of-mass (COM) received at the indicated UTC epoch. The reference point at A = Arecibo is the center-of-curvature of the 305 m antenna. The reference point at G = Goldstone is the intersection of the azimuth and elevation axes. Time-delay data weight of 1 μs is equivalent to 150 m accuracy, and 1 Hz in Doppler data weight corresponds to ∼63 mm/s in radial velocity at the 2380 MHz Arecibo S-band transmitter reference frequency, ∼17.5 mm/s at the 8560 MHz DSS-14 X-band transmitter reference frequency. The assigned measurement errors (err.) reflect imaging and frequency resolution, echo strength, and COM location uncertainty. Data from 2012 through Feb 2013 based on the new high-precision shape COM determinations and highlighted in **bold.** For completeness and consistency, we also list other available radar astrometry reported by Giorgini et al. (2008) as well as January 3, 5, 16, and March 15 visually estimated astrometry. The March 15 measurement has a range resolution of 150 m and was at the edge of detectability. Residuals (resid.) are the observed minus computed difference between the measurement and the prediction of the new ballistic orbit solution (see Fig. 7). "Nresid." is the residual normalized by dividing by the measurement uncertainty assigned by the observer.

were estimated by propagating the weighted least-squares solution formal measurement-covariance matrix from the solution epoch using numerically integrated variational partial derivatives that relate the state at an instant to the original epoch state.

We used two approaches in orbit fitting: a gravity-only model (solution 197) and a model that included non-gravitational acceleration components (Yeomans et al., 2004) that was intended to investigate if the Yarkovsky effect is detectable in the current astrometry data set (solution 199). We obtained a transverse acceleration (A2) proportional to heliocentric distance (1 au/r)^2 of $-5.59 \pm 2.20 \times 10^{-14}$ au d^{-2}. The relatively large uncertainty of this estimate agrees with and overlaps the $-5.1 \pm 2.8 \times 10^{-14}$ au d^{-2} estimate of Vokrouhlický et al. (2015) as well as zero, the gravity-only case, at 2.5σ. The additional degree of freedom in the solution also increases the high fractional-precision radar data's weighted residual mean and scatter by 8%, from 0.392 ± 0.504 to 0.424 ± 0.537, and decreases the residual χ^2 of the combined optical and radar post-fit dataset from 677.8 to 671.8 (−0.89%). Therefore, we do not consider non-gravitational acceleration (i.e., the Yarkovsky effect) detected by the revised and extended measurement dataset. The full measurement dataset remains well-described by ballistic motion over the 2004–2015 interval spanned by measurements.

Table 5 gives the radar astrometry with its post-fit observed minus computed residuals for the solution 197 ballistic trajectory. The osculating orbital elements and their uncertainties are summarized in Table 6. Fig. 7 shows position differences between the new and Giorgini et al. (2008) solutions and uncertainties in the solutions. The new ballistic solution is within 0.6σ of the Giorgini et al. prediction. Fig. 7 also shows the difference between the Giorgini et al. solution and a new solution that includes a non-gravitational acceleration. Our orbital analysis predicts that if a total position offset more than 8–12 km (or 9–37 μs in radar round-trip delay or 0.02–0.05 Hz in S-band Doppler shift) is measured in 2021 relative to the new ballistic prediction, and cannot be fit with the rest of the dataset, then it would be a deviation greater than the 3σ expectation from the ballistic model. This could be an evidence for the Yarkovsky effect.

7. Discussion

7.1. Implications of a bifurcated shape during the 2029 flyby

What are the implications of an elongated, possibly bifurcated shape for the 2029 flyby? Previous studies did not consider this particular shape, although Yu et al. (2014) assumed that Apophis

Table 6
Orbital elements and their uncertainties for the new ballistic orbital solution 197.

J2000 heliocentric IAU76 ecliptic coordinates Epoch 2,454,733.5 TDB = 2008 September 24.0 TDB		
Osculating element	Value	Formal 1σ
Eccentricity (e)	0.19119529(425)	0.00000000336
Perihelion distance (q)	0.74607243(853) au	0.00000000322 au
Perihelion date (TP)	2454894.91250(76582) d (2009 March 4.41251 TDB)	0.0000018133 d
Longitude of ascending node (Ω)	204.4460(284242)°	0.0000210642°
Argument of perihelion (ω)	126.4018(808361)°	0.0000206361°
Inclination	3.331369(22846)°	0.00000033093°
Semimajor axis (a)	0.922438300(9046) au	0.0000000001256 au
Orbit period, sidereal (P)	323.5969485(2066) d (0.885944636482 yr)	0.00000006607 d
Mean anomaly (M)	180.42938(5930)°	0.000002038°

The new ballistic orbit solution 197 for Apophis was estimated from a simultaneous weighted least-squares fit to 4435 optical astrometric pairs (R.A. & Dec.), spanning 2004 Mar. 15 to 2015 Jan. 3, 17 round-trip delay, and 29 Doppler frequency-shift measurements made from Arecibo and Goldstone in 2005−2006 and 2012−2013. The dynamical model includes the relativistic point-mass gravitational perturbations of the Sun, Newtonian point-mass perturbations of the planetary systems, Moon, 16 largest asteroids, and Earth J_2 oblateness when within 0.01 au. The solution epoch is in Barycentric Dynamical Time (TDB), the standard coordinate time of JPL's solar system ephemerides. The post-fit weighted R.A. observed minus computed residual mean is −0.007″ and Dec. residual mean is 0.011″, with a combined normalized rms of 0.275. The weighted delay mean residual is 0.271 ± 0.324 μs ms and the weighted Doppler mean residual is 0.282 ± 0.356 Hz. The combined optical and radar normalized residual rms for the dataset is 0.2757, with a residual χ^2 of 677.9. The coordinate system is defined by the DE431 planetary ephemeris solution, which is aligned within 0.0002″ of the quasar-based ICRF-2, with the x–y reference plane then rotated around the x-axis by the 84,381.448″ obliquity angle of the IAU76 convention to produce osculating elements referenced to the historical standard ecliptic plane.

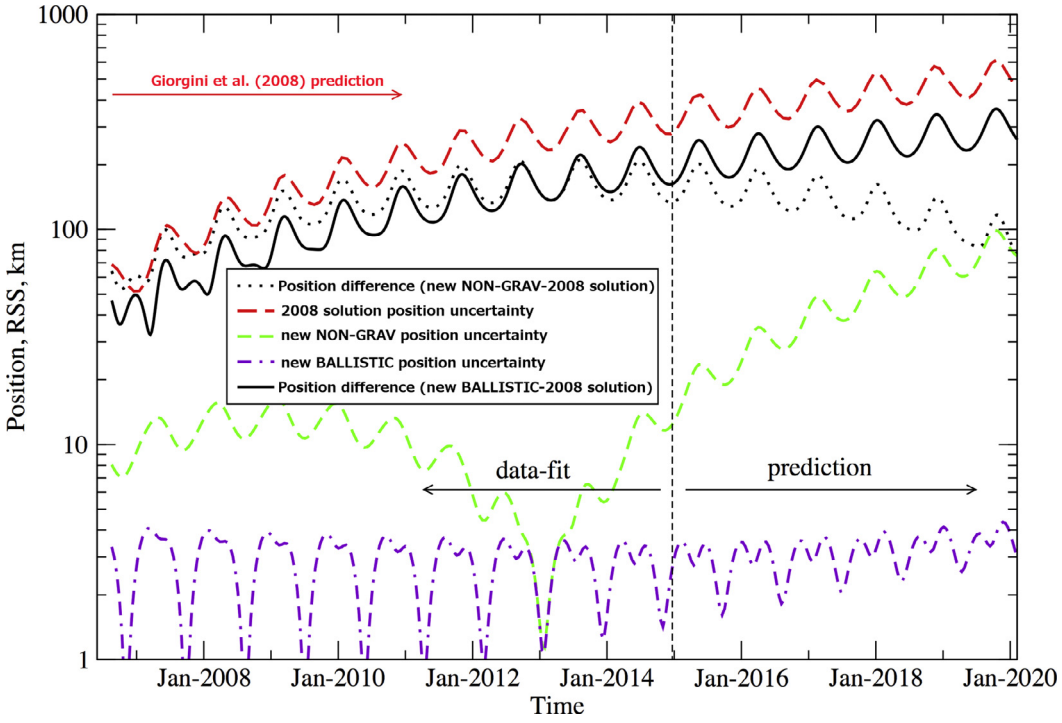

Fig. 7. Comparison of uncertainties and position differences between old and new numerically integrated orbit solutions for Apophis. Position differences and 1σ formal uncertainties in kilometers appear on the vertical axis as a function of time. The red curve is the 1σ position uncertainty of the old ballistic orbit solution, solution 142, from Giorgini et al. (2008). The purple curve gives the predicted 1σ position uncertainty of the new ballistic solution 197. The green curve is the predicted 1σ uncertainty of the new non-gravitational acceleration solution 199 (the Yarkovsky effect equivalent). The black solid curve is the heliocentric position difference obtained by subtracting the new ballistic solution from the Giorgini et al. (2008) ballistic solution. The black dotted curve is the position difference obtained by subtracting the new non-gravitational trial solution from the Giorgini et al. (2008) ballistic solution. Periodic oscillations in the curves are due to Apophis going through perihelion (with high rates of change) and aphelion (with lower rates of change). Optical and radar astrometry obtained in 2020−2021 is expected to reduce the uncertainties by at least one order of magnitude for subsequent predictions. (For interpretation of the references to colour in this figure legend, the reader is referred to the web version of this article.)

is an ellipsoidal rubble pile with a uniform or bimodal size of constituent particles. Yu et al. conducted numerical simulations to investigate if Apophis will undergo any internal and/or surface reshaping due to tidal interactions with the Earth. Their results indicated that tidal forces acting on the asteroid are weak, but that they may trigger small-scale surface avalanches. Large internal reconfiguration is unlikely, but even minor shifts in the interior could reconfigure regolith on the surface. Similar conclusions have been reached by Scheeres et al. (2005).

Binzel et al. (2010) investigated how the visible and near-infrared spectral characteristics of NEAs can change after the planetary encounters that occur within one lunar distance. They

showed that there is a statistically significant sample of Q-class NEAs that have un-weathered, young surfaces, that may be indicative of recent surface changes. Binzel et al. mentioned the Apophis encounter in 2029 as a potential direct test of tidally-induced surface modifications that could produce detectable changes in the asteroid's visible and near-infrared spectra and speculated that Apophis' spectral class could transition from weathered Sq to an un-weathered Q type.

It is possible that a bi-oblate shape could show more dramatic changes than a convex shape because of the higher angles of repose around the neck. A high-resolution radar imaging and orientation-selected spectral observations in 2029 might reveal changes.

7.2. Radar observations in 2021

The next opportunity for radar observations of Apophis will occur in March 2021 during an approach within 0.113 au. Apophis will be closer, 0.116 au, when it enters Arecibo's declination window than it was in February of 2013 (0.142 au). This should allow for delay-Doppler images with 15–30 m resolutions at three times stronger SNRs than in 2013.

The strongest SNRs at Goldstone in 2021 will be ~23/day, or about 70% of the SNRs that we obtained in 2013. We hope to receive with the 100 m Green Bank Telescope (GBT) on some days to increase the SNRs by a factor of two. We expect that the SNRs will be sufficient for 37.5 m resolution imaging. The 2021 radar data should enable improved estimation of the spin state and 3D shape. Radar ranging in 2021 is likely to show the effects of the Yarkovsky acceleration, and if so, enable estimation of the mass and bulk density.

7.3. Radar observations in 2029

Apophis will be an extremely strong radar target in 2029 at Goldstone and Arecibo. Goldstone observations of Apophis could start as early as mid-March and last until mid-May (Supplementary Table 2). High-resolution imaging (7.5 m and finer) would likely occur between April 4–24 when the SNRs exceed 100/run. We also plan to transmit at the 34 m DSS-13 antenna at Goldstone and receive at Green Bank and/or Arecibo, which should enable imaging at a resolution of 1.875 m/px.

Apophis will enter Arecibo's declination window on April 14 after the closest approach. The SNRs will be suitable for detailed imaging until late May (Supplementary Table 3). In principle, many other radar facilities around the world could observe Apophis in 2029 including DSS-43 in Australia, Kwajalein, Evpatoria, TIRA near Bonn, Germany, EISCAT near Tromso, Norway, Haystack Observatory in Massachusetts, and possibly others.

Scheeres et al. (2005) predicted that the spin state of Apophis is likely to change during the close encounter in 2029. A key objective driving the 2029 observations is to improve the 3D model and spin state using the data obtained before the close approach and then check for changes afterward. The flyby may also change small-scale surface features (Scheeres et al., 2005; Yu et al., 2014) that could be visible using high-resolution radar imaging.

Acknowledgments

We thank the Goldstone and Arecibo technical and support staffs for help with the radar observations. This work was performed at the Jet Propulsion Laboratory, California Institute of Technology, under contract with the National Aeronautics and Space Administration (NASA). This material is based in part upon work supported by NASA under the Science Mission Directorate Research and Analysis Programs and the Human Exploration and Operations Mission Directorate Advanced Exploration Systems Program. The work by P.P. and P.S. was supported by the Grant Agency of the Czech Republic, Grant 17-00774S. We would like to thank Davide Farnocchia, Steve Chesley, and Paul Chodas for a valuable discussion on the orbit of Apophis. We also thank two anonymous reviewers.

Supplementary materials

Supplementary material associated with this article can be found, in the online version, at doi:10.1016/j.icarus.2017.08.032.

References

Benner, L.A.M., et al., 2008. Near-Earth asteroid surface roughness depends on compositional class. Icarus 198, 294–304.
Binzel, R.P., et al., 2009. Spectral properties and composition of potentially hazardous Asteroid (99942) Apophis. Icarus 200, 480–485.
Binzel, R.P., et al., 2010. Earth encounters as the origin of fresh surfaces on near-Earth asteroids. Nature 463, 331–334.
Britt, D.T., Yeomans, D., Housen, K., Consolmagno, G., 2002. Asteroid density, porosity, and structure. In: Bottke, W., Cellino, A., Paolicchi, P., Binzel, R.P. (Eds.), Asteroids III. Univ. of Arizona Press, Tucson, pp. 485–500.
Brozovic, M., et al., 2017. Goldstone radar evidence for short-axis mode non-principal axis rotation of near-Earth asteroid (214869) 2007 PA8. Icarus 286, 314–329.
Delbo, M., et al., 2007. Albedo and size determination of potentially hazardous asteroids: (99942) Apophis. Icarus 188, 266–269.
Demura, H., et al., 2006. Pole and global shape of 25143 Itokawa. Science 312, 1347–1349.
Farnocchia, D., et al., 2013. Yarkovsky-driven impact risk analysis for Asteroid (99942) Apophis. Icarus 224, 192–200.
Giorgini, J.D., et al., 2008. Predicting the Earth encounters of (99942) Apophis. Icarus 193, 1–19.
Hogg, R.V., Tanis, E.A., 1993. Probability and Statistical Inference. Prentice Hall, New Jersey, USA, p. 218.
Hudson, S., 1994. Three-dimensional reconstruction of asteroids from radar observations. Remote Sens. Rev. 8, 195–203.
Licandro, J., et al., 2016. GTC/CanariCam observations of (99942) Apophis. Astron. Astrophys. 585, A10.
Magri, C., Consolmagno, G.J., Ostro, S.J., Benner, L.A.M., Beeney, B.R., 2001. Radar constraints on asteroid regolith compositions using 433 Eros as ground truth. Meteorit. Planet. Sci. 36, 1697–1709.
Magri, C., Ostro, S.J., Scheeres, D.J., Nolan, M.C., Giorgini, J.D., Benner, L.A.M., Margot, J.-L., 2007. Radar observations and a physical model of asteroid 1580 Betulia. Icarus 186, 152–177.
Mainzer, A.K., et al., 2011. NEOWISE observations of near-earth objects: preliminary results. Astrophys. J. 743, 156 17 pp.
Mitchell, D.L., et al., 1996. Radar observations of Asteroids 1 Ceres, 2 Pallas, and 4 Vesta. Icarus 124, 113–133.
Müller, T.G., et al., 2014. Thermal infrared observations of asteroid (99942) Apophis with Herschel. Astron. Astrophys. 566, A22.
Nolan, M.C., et al., 2013. Shape model and surface properties of the OSIRIS-REx target asteroid (101955) Bennu from radar and lightcurve observations. Icarus 226, 629–640.
Ostro S.J., et al., 1999. Asteroid 4179 Toutatis: 1996 radar observations. Icarus 137, 122–139.
Ostro, S.J., et al., 2004. Radar observations of asteroid 25143 Itokawa (1998 SF36). Meteorit. Planet. Sci. 39, 407–424.
Ostro, S.J., Hudson, R.S., Benner, L.A.M., Giorgini, J.D., Magri, C., Margot, J.-L., Nolan, M.C., 2002. Asteroid radar astronomy. In: Bottke, W.F., Cellino, A., Paolicchi, P., Binzel, R.P. (Eds.), Asteroids III. Univ. of Arizona Press, Tucson, pp. 151–169.
Pravec, P., et al., 2014. The tumbling spin state of (99942) Apophis. Icarus 233, 48–60.
Pravec, P., Harris, A.W., 2007. Binary asteroid population I. Angular momentum content. Icarus 190, 250–259.
Pravec, P., Harris, A.W., Kušnirák, P., Galád, A., Hornoch, K., 2012. Absolute magnitudes of asteroids and a revision of asteroid albedo estimates from WISE thermal observations. Icarus 221, 365–387.
Scheeres, D.J., Benner, L.A.M., Ostro, S.J., Rossi, A., Marzari, F., Washabaugh, P., 2005. Abrupt alteration of asteroid 2004 MN4's spin state during its 2029 Earth flyby. Icarus 178, 281–283.
Souchay, J., et al., 2014. Rotational changes of the asteroid 99942 Apophis during the 2029 close encounter with Earth. Astron. Astrophys. 563, A24.
Thomas, C.A., et al., 2011. ExploreNEOs. V. Average albedo by taxonomic complex in the near-Earth asteroid population. Astron. J. 142, 85 12 pp.
Vereš, P., Farnocchia, D., Chesley, S.R., Chamberlin, A.B., 2017. Statistical analysis of astrometric errors for the most productive asteroid surveys. Icarus 296, 139–149.

Vokrouhlický, D., et al., 2015. The Yarkovsky effect for 99942 Apophis. Icarus 252, 277–283.
Welch, P.D., 1967. The use of fast Fourier transforms for the estimation of power spectra: a method based on time averaging over short modified periodograms. IEEE Trans. Audio Electroacoust. 15, 70–73.
Yeomans, D.K., Chodas, P.W., Sitarski, G., Szutowicz, S., Krolikowska, M., 2004. Comets II. University of Arizona Press, pp. 137–151.
Yu, Y., et al., 2014. Numerical predictions of surface effects during the 2029 close approach of Asteroid 99942 Apophis. Icarus 242, 82–96.